[Short title + Author Name - P&H title] 17 (2024) 105929

Contents lists available at ScienceDirect

Arabian Journal of Chemistry

journal homepage: www.ksu.edu.sa

Original article

Regeneration of activated carbon by combined ultrasound and persulfate treatment

Shiwei Gao [a], Zheng Wang [a,*], Yannan Jia [b,c,*], Nannan Xu [b,c], Lisha Liao [b,c], Zhiwei Wang [a], Binbin Wu [a], Wanting Feng [a], Yuanxiang Shan [a], Lingpeng Hu [a], Hongqin Xue [a]

[a] College of Civil Engineering, Nanjing Forestry University, Longpan Road 159#, Nanjing 210037, China
[b] State Key Laboratory of Simulation and Regulation of Water Cycle in River Basin, China Institute of Water Resources and Hydropower Research, Beijing 100038, China
[c] China Institute of Water Resources and Hydropower Research, Beijing 100038, China

ARTICLE INFO

Keywords:
Ultrasonic
Persulphate
Regeneration
Carbonyl
Combined technology

ABSTRACT

In this study, the regeneration of waste activated carbon by the synergic combination of ultrasonication and persulfate treatment was explored. The regeneration efficiencies achieved with sonication and persulfate, both in combination and separately, were assessed from a sample's ability to adsorb ofloxacin before and after regeneration. The introduction of persulfate increased the regeneration rate by 4–5% over that of ultrasound alone, and the regeneration rate increased from 40.95 % to 45.71 % upon increasing the persulfate dosage from 1 to 10 mmol/L. Furthermore, the regeneration rate was found to be largely unaffected by pH. The specific surface area of the activated carbon regenerated by the combined technology was 527 m^2/g, which was 37 m^2/g higher than that for ultrasonic regeneration alone, further demonstrating the utility of the combined approach. In summary, combined ultrasonication/persulfate regeneration provides a practical and cost-effective method for the reuse of waste activated carbon.

1. Introduction

The management of pollutants is currently receiving significant attention from the scientific community, with antibiotics, as a relatively new class of pollutant (Harrower et al., 2021), being of particular interest. For instance, fluoroquinolone antibiotics such as ofloxacin (OFX) have been detected in near-sea areas (Faris et al., 2021), rivers and lakes, drinking water, and surface water in China. If such substances persist in water environments for long periods of time (Chen et al., 2022), they can lead to resistant pathogen strains and/or form composite pollutants with other waterborne substances, such as heavy metals and microplastics, negatively affecting the safety of aquatic ecosystems (Chen et al., 2020; Robles-Jimenez et al., 2021).

Adsorption technologies based on highly porous solid materials with high specific surface areas, such as activated carbon, zeolites, and alumina, are considered a promising means of removing pollutants from environmental water owing to their low cost, safety, high efficiency, and environmental friendliness (Guillossou et al., 2019; Liu et al., 2020).

Activated carbon has a very high specific surface that is area rich in functional groups, making it highly suitable for the adsorption and removal of various pollutants (Baby and Prakash, 2005; Cheng et al., 2021) including large organic pollutants, effectively lowering chemical oxygen demand concentrations (Beker et al., 2010). The adsorption effect of activated carbon varies depending on its particulate nature and pore structure. The main disadvantage of antibiotic adsorption with activated carbon is that it produces a large amount of polluted carbon waste (Rodrigues et al., 2011), which presents both economic and environmental problems. However, research into the regeneration and reuse of activated carbon remains in its infancy, (Spessato et al., 2019; Sanchez-Yepes et al., 2023).

Methods for the regeneration of activated carbon are mainly based on thermal treatment, ultrasonication (Sun et al., 2018), electrochemical treatment (Zhang, 2002), supercritical fluid treatment (Salvador et al., 2013), microwave regeneration (Ge et al., 2018) and advanced oxidative regeneration (Benhamed et al., 2016). In recent years, the regeneration of activated carbon using ultrasonic cavitation has seen good progress, and its use in combination with other techniques to regenerate saturated activated carbon has become an active area of

* Corresponding authors at: College of Civil Engineering, Nanjing Forestry University, Longpan Road 159#, Nanjing 210037, China (Z. Wang); State Key Laboratory of Simulation and Regulation of Water Cycle in River Basin, China Institute of Water Resources and Hydropower Research, Beijing 100038, China (Y. Jia).
E-mail addresses: wangzheng@njfu.edu.cn (Z. Wang), jiayn@iwhr.com (Y. Jia).

https://doi.org/10.1016/j.arabjc.2024.105929
Received 19 April 2024; Accepted 22 July 2024
Available online 29 July 2024

research (Pang et al., 2011).

Ultrasonic waves are sound waves with a frequency of more than 16 kHz that, in a liquid, are transmitted in the form of spherical waves (Chowdhury and Viraraghavan, 2009). The degradation of pollutants in wastewater by ultrasonic waves is mainly based on ultrasonic cavitation, where the local temperature and pressure can reach around 5000 K and 50 MPa, respectively, when a "cavitation bubble" collapses (Jiang et al., 2002). When a saturated adsorbent is exposed to such high temperature and pressure, the energy generated will be transferred to the adsorbate, imparting sufficiently intense thermal movement to detach it from the surface of the adsorbent and enter the solution (Mahamuni and Pandit, 2006). The factors affecting ultrasonic regeneration of activated carbon are mainly pH, ultrasonication intensity, ultrasonication treatment time, and ultrasonication temperature.

Advanced oxidation technologies based on the generation of reactive free radicals with strong oxidizing properties have been widely used in the field of environmental remediation (Waclawek et al., 2017), and the use of advanced oxidation techniques for the regeneration of adsorbents has received widespread attention since it was first reported by Mourand (Mourand et al., 1995). The main advanced oxidation techniques used for regeneration of adsorbents involve photocatalytic oxidation, Fenton oxidation, activated persulfate oxidation, and ozone oxidation (Yin et al., 2020). Advanced oxidation technologies based on sulfate radicals ($SO_4^{\bullet-}$) have become an active area of research in recent years. $SO_4^{\bullet-}$ can be generated using UV, heat, strong bases, ultrasonication, transition metal ions, and has a strong oxidizing ability (Wang et al., 2015; Miklos et al., 2018). The most common persulfates are permonosulfate (PMS) and perdisulfate (PDS), with the main source of PMS being potassium peroxymonosulfate complex salt ($2KHSO_5$-$KHSO_4$-K_2SO_4), whose active component is HSO_5^-, and the active component of PDS is $S_2O_8^{2-}$, the sodium salt of which is commonly used (Wang and Wang, 2020). Unlike H_2O_2, persulfate is solid at room temperature, making it easy to store and transport, and it is highly stable and water soluble, all of which are advantages in terms of its application to pollutant degradation and adsorbent regeneration (Lee et al., 2020).

Despite the numerous technologies available for the regeneration of saturated activated carbon, only thermal regeneration technology has been applied in actual water plants (Ersan et al., 2023). Although thermal regeneration technology can effectively restore the adsorption capacity of activated carbon, the regeneration process consumes large amounts of energy and material loss is significant, resulting in high operating costs (Gomez-Rueda et al., 2022). Therefore, other economical, environmentally benign, and high-efficiency methods for the regeneration of activated carbon are required (Zhang et al., 2023).

The regeneration of activated carbon by persulfate oxidation achieves complete degradation of the adsorbate on activated carbon in an environmentally friendly and economic manner, but it requires prolonged regeneration times and is subject to low regeneration rates (Sanchez-Yepes et al., 2023). The ultrasonic regeneration of activated carbon exhibits the advantages of good desorption effect, fast regeneration rates (Ye et al., 2022), and the non-destruction of the adsorbent. Furthermore, unlike traditional advanced oxidation agents such as H_2O_2 and O_3, persulfate is stable and easily stored and transported (Babuponnusami and Muthukumar, 2014). Furthermore, the redox potential of sulfate radicals ($SO_4^{\bullet-}$) produced by persulfate is higher than that of hydroxyl radicals ($HO^{\bullet}$) produced by H_2O_2 or O_3; the half-life of $SO_4^{\bullet-}$ is longer than that of $HO^{\bullet}$; and $SO_4^{\bullet-}$ is more selective and pH independent than $HO^{\bullet}$ (Matzek and Carter, 2016). Ways of activating persulfate include heating, UV, ultrasonication, microwave radiation, strong bases, transition metals, and carbon activation. Among them, ultrasonication can break the peroxygen bond of persulfate and generate $SO_4^{\bullet-}$ (Zhao et al., 2021), while the high energy generated by ultrasonic waves detaches the adsorbate from the surface of activated carbon into the solution, where it can be degraded by free radicals. This method does not involve additional materials or secondary pollution, which is a key factor in its popularization and application (Chen et al., 2022).

This study focuses on combining the advantages of ultrasonication and PDS (US/PDS) oxidation for the regeneration of activated carbon. PDS oxidation is unable to regenerate the deeper carbon micropores; however, making use of the cavitation vibrations caused by ultrasonication more effectively desorbs pollutants adsorbed into the mesopores and micropores in activated carbon, allowing the organic matter desorbed into the regeneration solution to be removed through the synergistic effect of US/PDS oxidation, so as to improve the regeneration efficiency of the entire process while keeping microporous structure of the activated carbon undamaged. This new US/PDS strategy allows regeneration of saturated activated carbon that is highly efficient, green, economical, and energy-saving, providing a feasible solution for both the popularization and cost-reduction water treatment using activated carbon.

2. Materials and methods

2.1. Experimental reagents and materials

For this study, granular activated carbon was produced by Inner Mongolia Taixi Coal Chemical Co. Ltd., while OFX ($C_{18}H_{20}FN_3O_4$), sodium hydroxide (NaOH), hydrochloric acid (HCl), methanol (CH_4O), ethanol (C_2H_6O), *tert*-butanol ($C_4H_{10}O$), and potassium persulfate ($K_2S_2O_8$) were purchased from Nanjing Chemical Reagent Co. Information on waste activated carbon is added to the supplementary materials.

2.2. Experimental characterization

The specific surface areas and pore structures of new, used, and regenerated carbon were determined from Brunauer–Emmet–Teller (BET) N_2 adsorption–desorption (Micromeritics, ASAP 2020, USA) Their functional groups were explored by Fourier transform infrared (FTIR) spectrometry (Frontier, PerkinElmer, USA). X-ray diffractometry (XRD; PANalytical Empyrean, The Netherlands) and Raman spectrometry (Renishaw inVia-Reflex, UK) were used to explore the carbonaceous structures and constituents of the activated carbons. Milled powder samples were pressed with KBr as a carrier, and their surface compositions were characterized by X-ray photoelectron spectroscopy (XPS; PHI 5700 ESCA system, USA). Bonding energy (BE) values were scaled according to the adventitious C1s peak at 284.8 eV. The morphologies of the samples were observed using scanning electron microscopy (SEM; JSM-7401F). A particle size analyzer (Mastersizer 3000, Malver Panalytical UK) was used to determine the particle sizes of the samples. OFX degradation intermediates were analyzed by HPLC-MS (Ultimate 3000 UHPLC-Q Exactive, Thermo Scientific, US). The organic compositions of water samples were determined using a three-dimensional fluorescence spectrometer (F7000, HITACHI, Japan). Determination of the free radical species in water was performed using electron paramagnetic resonance (EPR; JES-FA200 Nippon Electron Co.).

2.3. Regeneration setup and procedures

The regenerator setup is shown in Fig. 1. An immersion ultrasonic probe was used for the regeneration experiments. The reactor was constructed from a 2000 mL beaker. The ultrasonic transducer bar probe diameter was 60 mm, the transducer operating frequency was 40 kHz, and the base was a magnetic stirrer. Adsorption-saturated activated carbon, a certain amount of potassium persulfate, and the rotor were added to the beaker. The ultrasonic and stirring devices were activated to initiate the reaction, and at the end of the reaction, the regeneration solution was poured off, and the remaining moist regenerated activated carbon was put into an oven at 80 °C for 2 h for ventilation and drying.

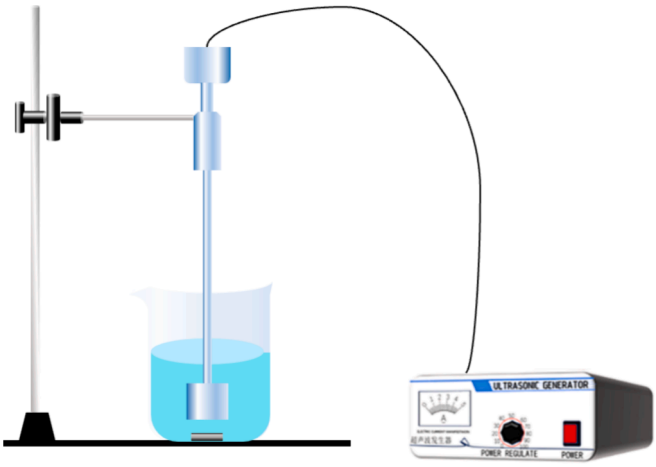

Fig. 1. Regenerator setup.

2.4. Analysis of data

The regeneration efficiency (E) was calculated by comparing the adsorption capacities of the activated carbon before and after regeneration, as shown in Eq. (1). And the adsorption capacity Q_0 (mg/g) is calculated from Eq. (2).

$$E = Qr/Qm \times 100\% \quad (1)$$

where E is the regeneration efficiency, Q_r is the adsorption capacity of the activated carbon after regeneration (mg/g), and Q_m is the adsorption capacity (mg/g) of the fresh activated carbon. for the same concentration of adsorbent.

$$Q0 = \frac{(C0 - Ce)V}{M} \quad (2)$$

Where Q_0 is the adsorption capacity of the activated carbon; C_0 and C_e are the initial and equilibrium concentrations of ofloxacin (mg/L), respectively; V is the volume of the solution (L); and m is the mass of activated carbon (g);

3. Results and discussion

3.1. Characterization of activated carbon samples

In order to investigate the effect of ultrasonic regeneration on the surface morphology and pore structure of the activated carbon, it was characterized by SEM before and after regeneration. In this section, AC-1, AC-2, AC-3, AC-4 represent new carbon, waste activated carbon, ultrasonically regenerated carbon, and US/PDS regenerated carbon, respectively. As shown in Fig. 2**a**, the surface pores of the new carbon are well developed, with rough pore walls, clear microporous, mesoporous, and macroporous structures, and uniform distribution. As shown in

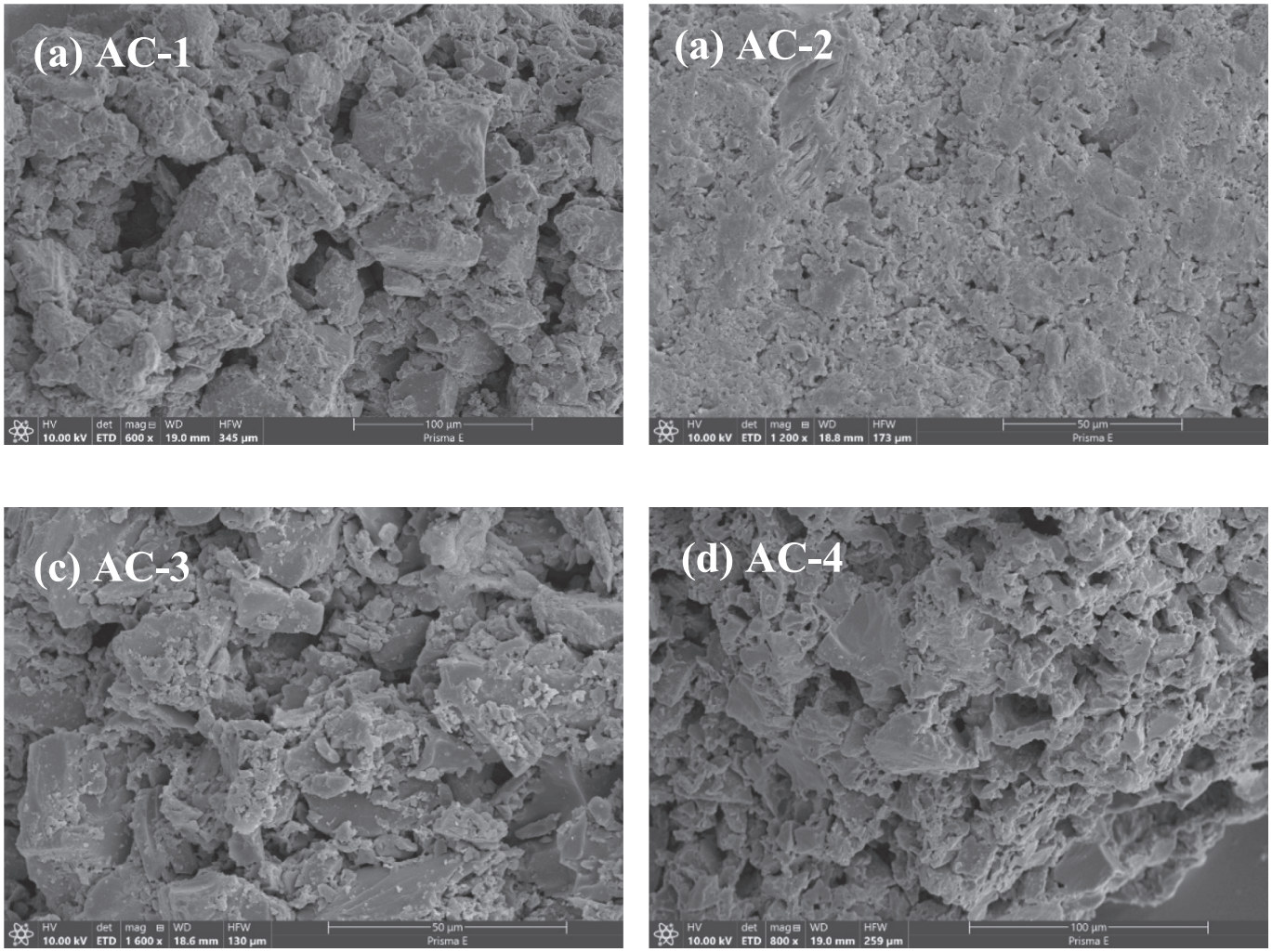

Fig. 2. SEM images of (a) AC-1, (b) AC-2, (c) AC-3, and (d) AC-4.

Fig. 2**b**, the original uneven pores of the activated carbon are blocked by the adsorbate, and the surface is smooth, with part of the micropore and mesopore structure still visible. As shown in Fig. 2**c**, after ultrasonic regeneration, the internal pores of the activated carbon are partly exposed, and its adsorption capacity has been restored to a certain extent. As shown in Fig. 2**d**, the OFX coating film has been destroyed by US/PDS regeneration to a greater extent, more activated carbon pores are exposed, and the adsorption capacity of the activated carbon is further restored.

The degrees of graphitization and defects for carbonaceous materials can be determined by Raman spectroscopy. Generally speaking, the intensity ratio of the D band to the G band (I_D/I_G) reflects the degree of defects, with higher ratios indicating a higher degree of defects (Sadezky et al., 2005). As shown in Fig. 3**a**, I_D/I_G for pristine activated carbon is 1.210, and after saturation with OFX, it is 1.065, indicating that the degree of defects decreases with occupation of the activated carbon pores by OFX molecules. After ultrasonic regeneration, the I_D/I_G ratio is 1.128, indicating that the number of defects in the activated carbon has increased, and after US/PDS regeneration, the I_D/I_G ratio is 1.187, indicating that defects of the activated carbon are enhanced by the use of persulfate, which further indicates that compared with ultrasonic regeneration alone, the US/PDS regeneration achieves further recovery

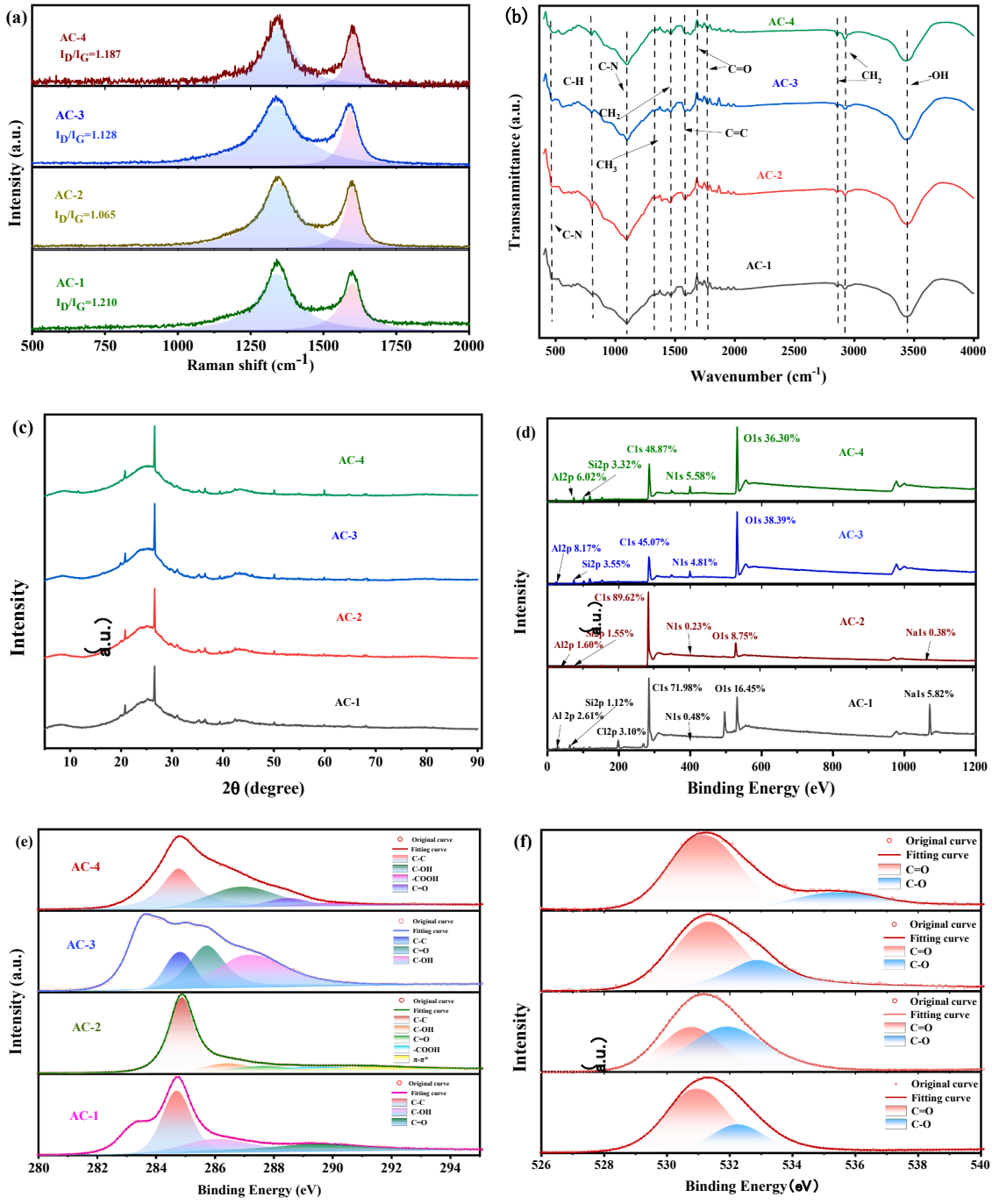

Fig. 3. Structural characterizations of AC-1, AC-2, AC-3, and AC-4. (a) Raman spectra. (b) FTIR spectra. (c) XRD spectra. (d) XPS survey. (e) Deconvoluted C1s spectrum. (f) Deconvoluted O1s spectrum.

of adsorption performance (Wang et al., 2019).

FT-IR characterizes the functional groups on the surface of activated carbon material, which are important for the chemisorption of OFX (Jiang et al., 2021). In Fig. 3**b**, the characteristic peak located at 3424 cm^{-1} is the —OH stretching vibration peak, and the absorption peak at 1587 cm^{-1} is mainly due to C═C vibration. The characteristic peak at 796 cm^{-1} is due to the C—H bending vibration of the benzene ring, and there is no significant intensity difference between the pristine and re-generated samples for these functional groups. The stretching vibration signals for nitrogen-containing groups are located at 1089 cm^{-1} (amine C—N) and 467 cm^{-1} (amine C—N), respectively (Huang et al., 2019). The intensity of these signals for the regenerated activated carbon

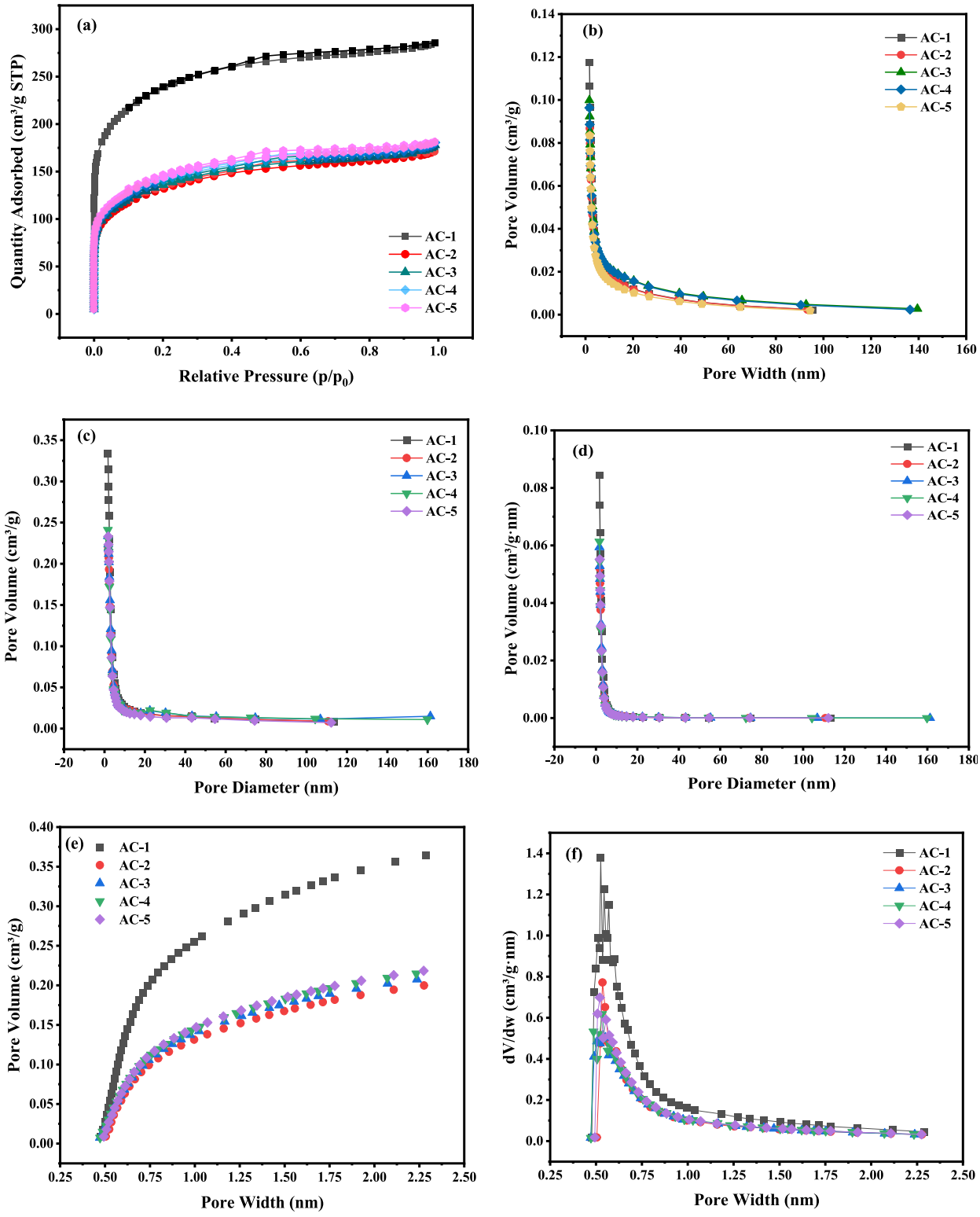

Fig. 4. (a) N_2 adsorption–desorption isotherms; BJH mesopore pore size distributions. (b) Cumulative pore volume-pore size distribution. (c) dV/dD-aperture variation graphs. (d) dV/dlog(D) plot of pore size variation; H-K micropore size distributions. (e) Cumulative micropore volume-pore size distribution diagram. (f) dV/dD-pore size change diagram.

samples are decreased, indicating that the nitrogenous groups are disrupted by ultrasonic regeneration to some extent.

XRD analysis can further demonstrate the evolution of the microstructure, as shown in Fig. 3**c.** The (002) and (100) crystal planes of carbon mainly show as two broad amorphous diffraction peaks (Wang et al., 2019), indicating that the samples have typical amorphous carbon structures with more graphite-like structures. The intensities of the diffraction peaks for the pristine and regenerated samples are similar. This indicates that the cavitation effect of ultrasound has no effect on the structure of activated carbon, further demonstrating its practical application value. Meanwhile, the two characteristic peaks also characterize the active sites on the surface of the activated carbon as well as the degree of defects, reflecting the excellent adsorption performance of activated carbon.

The surface chemistry and structures of ACs were also investigated (Huang et al., 2017). XPS was used to compare the elemental compositions of the surfaces of the activated carbon before and after regeneration. The survey spectrum in Fig. 3**d** shows that the samples mainly contain C, O, N, Al, and Si, where peaks occurring in the range 290–280 eV are C1s peaks, those in the range 538–528 eV are O1s peaks, and those in the range 403–397 eV are N1s peaks.

The XPS results show that C and O are the main elemental components of the samples. As shown in Fig. 3**d** the C contents decrease from 71.98 % in AC-1 and 89.63 % in AC-2 to 45.07 % in AC-3 and 48.87 % in AC-4, and the corresponding O contents increase from 16.45 % and 8.75 % to 38.39 % and 36.30 %, which could be attributed to destruction of the activated carbon surface by ultrasonication. As shown in Fig. 3**f**, the abundance of oxygen-containing functional groups on the surface increases to a certain extent after regeneration, so it can be inferred that there is a destruction of covalent bonds formed between carbon atoms by the cavitation effect of ultrasonic waves and that covalent bonds are formed between carbon atoms and other elements. Furthermore, it can be observed from the O1s spectra (Jeon et al., 2013) that the proportion of C═O in the regenerated activated carbon is increased; while, the C1s spectrum **(**Fig. 3**e)** after deconvolution shows that the surface chemistry and disordered or defective nature of sample surface are different before and after regeneration, suggesting that ultrasonication effects these properties (Sun et al., 2021).

To explore any changes in the activated carbon pore structure upon different regeneration treatments, fresh carbon (AC-1), waste activated carbon (AC-2), samples after ultrasonic regeneration for 10 (AC-3) or 30 min (AC-4), and US/PDS regenerated carbon (AC-5) were subjected to BET and BJH analyses (Gao et al., 2020). Fig. 4**a** shows the N_2 adsorption/desorption isotherms of the five samples. N_2 adsorption is mainly concentrated in the range of low relative pressure ($P/P_0 < 0.2$), and there is a I-type hysteresis loop in the range 0.4–1, indicating that the activated carbon has a predominantly microporous structure, which is believed to be favorable for the transport of liquid molecules.

According to the data of specific surface area and pore volume and pore diameter in Table 1, the specific surface area of saturated activated carbon was 483.357 m^2/g, and the specific surface area of carbon after regeneration by synergistic technology was 627.42 m^2/g, which recovered 29.8% relative to saturated carbon, respectively. The specific surface area of micropores and mesopores of the regenerated carbon were recovered to some extent, but the microporosity and microporosity were not significantly different from those of the new carbon and the waste carbon.

The distribution of mesopore volume and pore size of the five kinds of activated carbon were obtained by the BJH method, and Fig. 4**b** shows dV/dD plotted as the vertical coordinate, where a higher value indicates that the number of pores corresponding to that pore size is higher.

Fig. 4**c** is plotted with dV/dlog(D) as the vertical coordinate to magnify the pore size distribution in the nanometer range. Fig. 4**d** show that the mesopores of the five samples have a uniform peak at 3–7 nm, indicating that their pore sizes are mainly distributed in this range. The mesopores of the new and saturated samples are mainly concentrated in the 4.3–6.7-nm range, while those of the ultrasonically regenerated samples are mainly concentrated in the 3.8–5.6-nm range, showing that the mesopore distribution range decreases upon regeneration. Furthermore, there may be some expansion of mesopores into micropores, which leads to a general decrease in the distribution of mesopores after regeneration.

Fig. 4**e** shows the cumulative micropore volume-pore size distribution, which shows that the number of micropores with volumes in the range 0.5–2 nm increases with increasing pore size. The cumulative pore volume in the range 0.8–2 nm is higher after regeneration than that of the waste activated carbon, which indicates that the content of larger micropores increases upon ultrasonic regeneration.

Fig. 4**f** characterizes the pore size distribution of activated carbon micropores with pore size as the horizontal coordinate and dV/dD as the vertical coordinate to illustrate the change of pore volume. When dV/dD corresponding to a certain horizontal coordinate in the figure is higher, the number of pores corresponding to that pore size is higher. The five samples show a clear peak at 0.5–0.6 nm, so the micropores are mainly distributed in this range.

3.2. *Performance factors for ultrasonic regeneration alone*

3.2.1. *Regeneration performance at different power levels*

The regeneration of activated carbon was performed at ultrasonication powers of 90, 150, 210, and 270 W. As shown in Fig. 5, the increase in power has a promoting effect on regeneration efficiency. When the power is 270 W, the regeneration efficiency decreases after 20 min, do it can be inferred that to achieve the same regeneration efficiency, lower-power ultrasonic waves need to act for a longer time, and high-power ultrasonic waves need to act for a short period of time, but the effect is not linear.

When the power is more than a certain value, the surface of the sonication source will produce a large number of useless bubbles, hindering the propagation of ultrasound waves and scattering their energy, which is not conducive to adsorbate removal. In addition, increasing the power will cause damage to the surface structure of the activated carbon, especially the microporous structure, so 210 W was chosen as the optimal power in this study.

Table 1
Pore structure parameters of different carbon samples.

Carbon type	Specific surface area (m^2/g)			Pore Volume(cm^3/g)		Pore Size (nm)
	S_{Bet}	S_{mic}	S_{mes}	Vmic (H-Ka)	Vmes (BJHb)	Da (DFTc)
New carbon	881.034	438.434	442.599	0.443123	0.174037	2.0118
Saturated carbon	483.357	180.379	302.978	0.265431	0.070658	2.1966
US-10 min	560.928	184.463	306.464	0.277566	0.077065	2.2616
US-30 min	595.583	188.024	313.559	0.282265	0.081285	2.2782
US + PDS	627.418	209.860	317.558	0.290587	0.082884	2.1280

a H-K: Numerical calculation of microporous pore size distribution by the Horvath-Kawazoe method.
b BJH: Values calculated from mesopore distributions by the Barrett-Joyner-Halenda method.
c DFT: Values calculated from density functional theory pore size distributions.

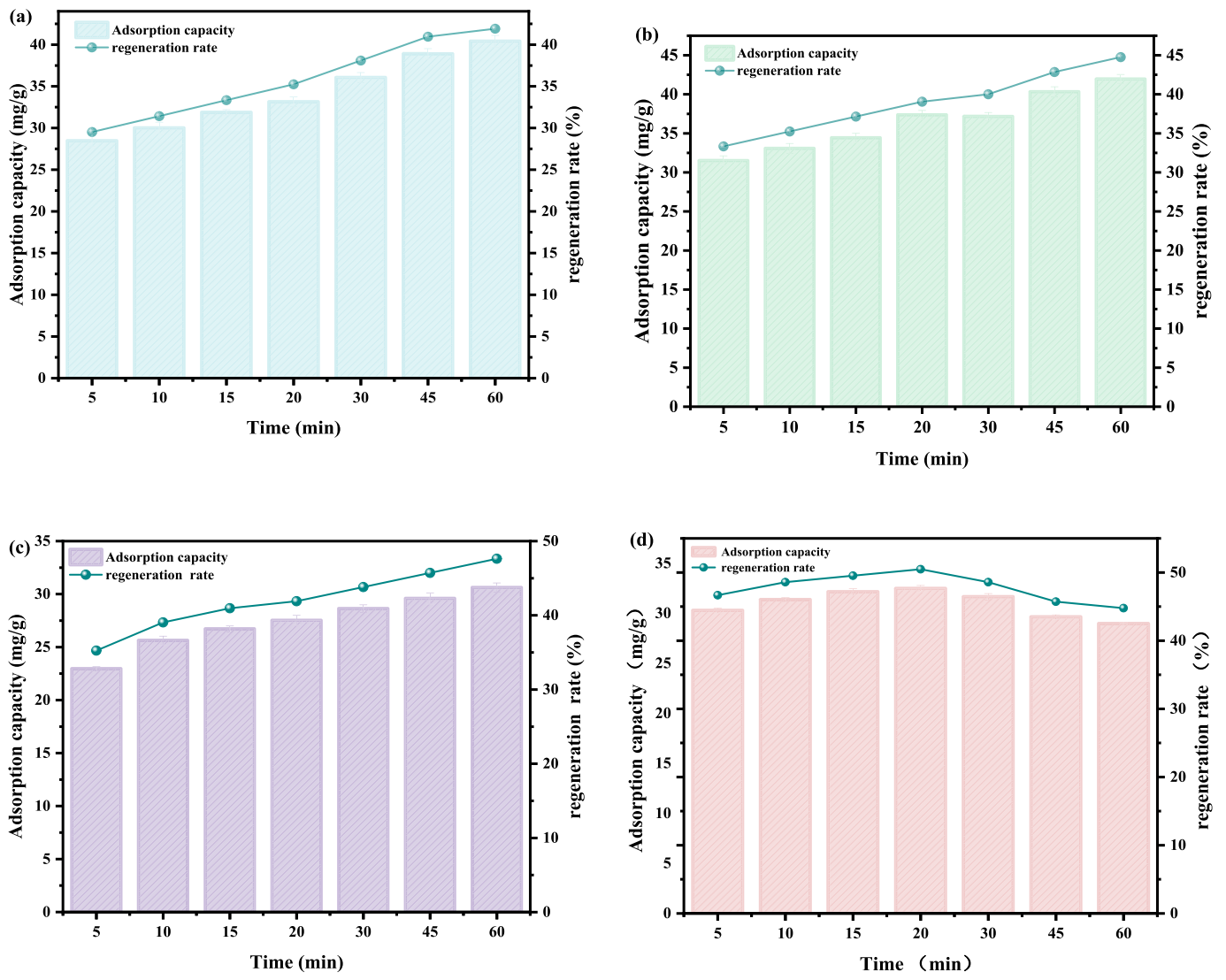

Fig. 5. Adsorption capacities and regeneration rates under different ultrasonication powers. (a) 90 W, (b) 150 W, (c) 210 W, (d) 270 W.

Furthermore, it can be observed from the Fig. 5 that the regeneration efficiency increases with the prolongation of ultrasonication time, and the increase in regeneration efficiency per unit time period decreases with increasing regeneration time. The regeneration efficiency increases rapidly before 20 min; after which it can reach 47.61 %, but the regeneration rate is slower, which is because the regions of the activated carbon surface susceptible to ultrasonic cavitation reach equilibrium. At this point, the diffusion of the adsorbate from the inside of the adsorbent to the outside becomes the limiting step of ultrasonic regeneration. Thus, we concluded that the optimum ultrasonic action time was 20 min.

3.2.2. Regeneration performance under different conditions

The effects on regeneration efficiency of pH, activated carbon particle size, activated carbon dosage, and the number of times the regeneration solution is replaced were investigated at a power of 210 W and 20 min regeneration time.

According to Fig. 6**a**, the regeneration efficiency slowly increases with pH value when the pH value is less than 7. The highest regeneration rate is 40 % at pH 7, and it is 36.19 % at pH 3, which is a difference of only 3.71 %. The regeneration efficiency decreases to 35.23 % at pH 11, which is a difference of only 1.97 % from the optimal value. Thus, ultrasonic regeneration is not particularly affected by pH.

According to Fig. 6**b**, the particle size of the activated carbon sample has a significant influence on regeneration by ultrasonic waves. When the particle size is between 30 and 50 mesh, the ultrasonic regeneration rate is 32.38 %, and when the particle size is less than 20 mesh, the ultrasonic regeneration rate is 13.33 %, which is a difference of 19.05 %. Overall, a decrease in particle size favors the regeneration effect of ultrasonic waves on activated carbon. This is mainly due to the fact that ultrasonic waves propagate in the form of spherical waves in the medium, and the collision with the pore wall when propagating into the curved hole will cause energy loss. The activated carbon with large pore size has more curved holes inside, so the energy loss is also more, which is the main reason why ultrasonic waves have better regeneration effect on activated carbon with small particle size and large specific surface area.

An increase in the dosage of saturated activated carbon decreases the regeneration efficiency of the activated carbon according to Fig. 6**c**, but the decrease is small. Upon increasing from 5 to 15 g, the regeneration rate decreases by only ~ 4 %, which demonstrates that ultrasonic regeneration is not affected by the particle concentration due to the propagation characteristics of the waves. Within a certain dosage range, the ultrasonic waves form cavitation by compression and release of gases generated on the pore surface of the activated carbon, and this effect can be transmitted to the pore surface of the activated carbon.

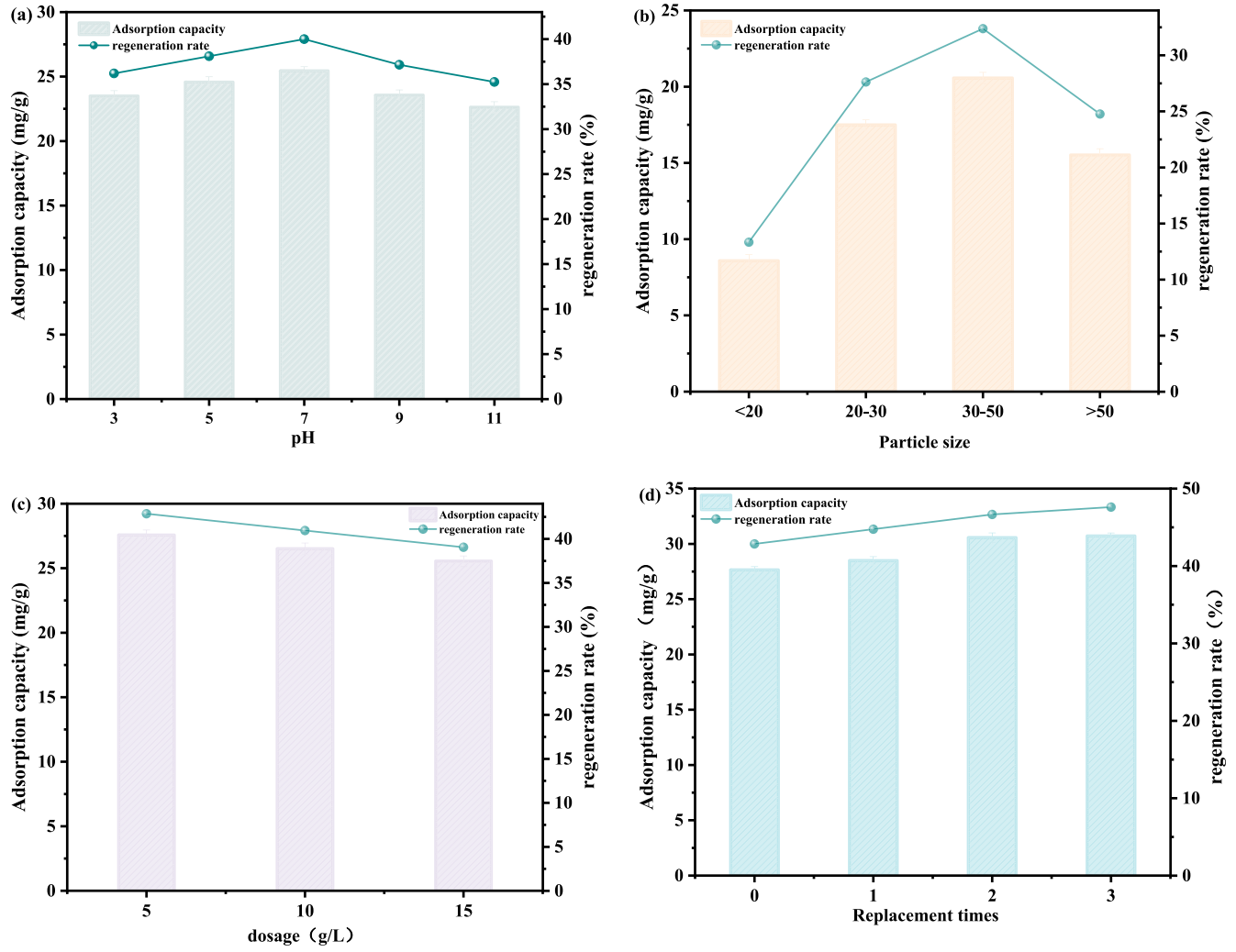

Fig. 6. Influence of (a) pH, (b) particle size, (c) dosage, (d) solution replacement on adsorption capacity and regeneration rate for ultrasonic regeneration.

According to Fig. 6**d**, the regeneration efficiency can be improved by changing the water, but the improvement is not significant. The regeneration rate increases by 4.76 % for three fluid changes compared with that for one fluid change.

3.3. *Performance factors for US/PDS regeneration*

The dosage of of PDS and pH were investigated. As shown in Fig. 7**a**, the regeneration rate increases with PDS dosage up to 10 mmol/L, at which the regeneration rate is 45.71 %. With further increase of PDS dosage, the regeneration rate decreases, reaching 43.80 % when the PDS dosage is 20 mmol/L. Ultrasonication activation enables PDS to produce $SO_4^{\bullet-}$, which can degrade the OFX that has been physically desorbed by the ultrasonic waves, preventing its re-adsorption and shifting the adsorption equilibrium favorably. However, with further increase in the concentration of PDS, the quenching of free radicals decreases the degradation rate, as excess PDS can react with free radicals. Therefore, the optimum PDS concentration for this system was determined to be 10 mmol/L.

As shown in Fig. 7**b**, the regeneration rates were compared under different pH conditions. The regeneration rate under basic conditions reaches 40.68 %, under acidic condition it reaches 41.13 %, and under neutral condition it reaches 43.80 %. This may be due to the fact that under acidic conditions, some of the PDS may not be directly activated to produce sulfate radicals, but is directly consumed in the solution (Eqs. (2)–(4)) whereas, under alkaline conditions, the •OH is not as oxidizing as $SO_4^{\bullet-}$ because the $SO_4^{\bullet-}$ produced by ultrasonic activation reacts with hydroxide radicals in the solution to produce •OH, which has a redox potential lower than that of $SO_4^{-}\cdot$, and thus the oxidizing property of •OH is not as good as $SO_4^{-}\cdot$(Wang and Jian 2015), and thus the activated carbon is not as oxidizing as $SO_4^{-}\cdot$, and thus the regeneration rate of activated carbon decrease (Eqs. (5)–(6)). However, overall, the difference in regeneration effect is not particularly large as the regeneration environment changes from acidic to alkaline. This demonstrates that the US/PDS method has good applicability over a wide range of pH conditions. In practice, the pH range of industrial wastewater varies greatly; therefore, this regeneration method has good practicality and engineering prospects.

Fig. 7**c** and Fig. 7**d** show a comparison of adsorption capacity and regeneration rate for regeneration by ultrasonic and US/PDS processes, respectively, for different powers. Clearly, adsorption capacity and regeneration rate are increased by the introduction of persulfate.

$$S_2O_8^{2-}+H^+\rightarrow H_2SO_8\rightarrow HSO_4^-+SO_4^{2-} \quad (2)$$

$$SO_4^{2-}+H_2O \rightarrow HS_2O_5^- \quad (3)$$

$$SO_4^{2-}\rightarrow SO_3^{2-}+1/2O_2 \quad (4)$$

$$SO_4^-\cdot+OH^-\rightarrow SO_4{}^{2-}+\bullet OH \quad (5)$$

$$SO_4^-\cdot+H_2O\rightarrow \bullet OH + SO_4{}^{2-}+H^+ \quad (6)$$

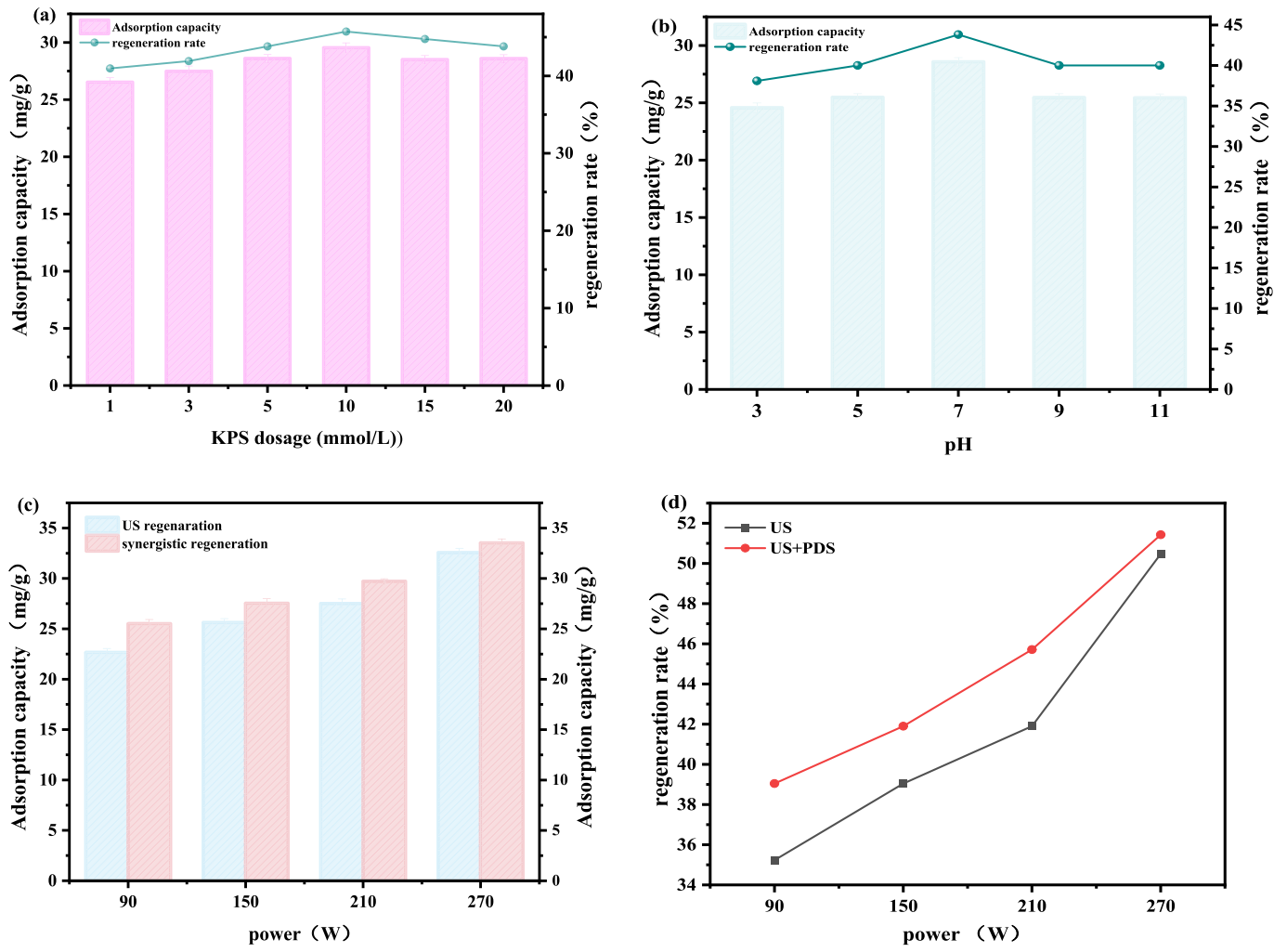

Fig. 7. The effects (a) PDS dosage and (b) pH on adsorption capacity and regeneration rate for the US/PDS system. Effect of power on (c) adsorption capacity and (d) regeneration rate for ultrasonication and US/PDS regeneration.

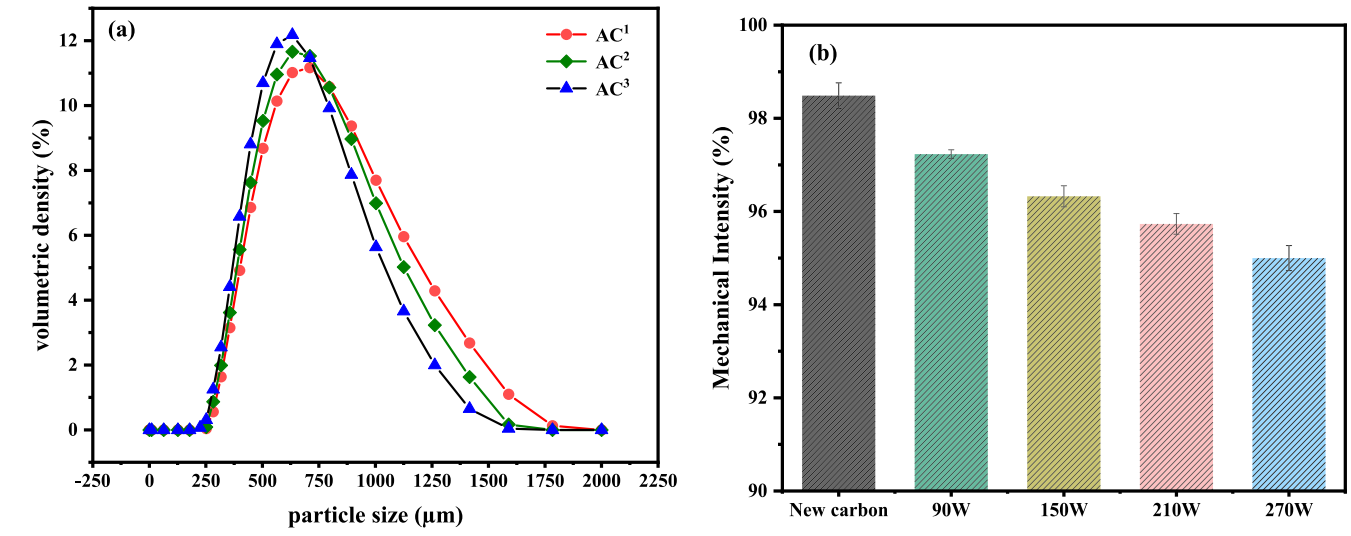

Fig. 8. (a) Particle size distributions of different regenerated samples. (b) Changes in the mechanical strength strength of samples under different ultrasonication power conditions.

3.4. Particle size distribution and mechanical strength changes of different regenerated samples

Fig. 8**a** shows the particle size analysis results for new carbon, ultrasonically regenerated carbon, and US/PDS-regenerated carbon. In the figure, AC^1, AC^2, and AC^3 represent new carbon, ultrasonically regenerated carbon, and ultrasonic-peroxysulfate synergistic regeneration, respectively. There is a certain degree of difference in the distributions of particle size before and after regeneration. After regeneration, the particle size distribution curve shifts to the left as a whole, which indicates that the particle size is uniformly reduced, and the particle size is obviously reduced in the range of 750–1500 μm. From the particle size distribution data in Table 2, the surface area particle size of activated carbon regenerated by ultrasonic waves has an average particle size of 580 μm, and that of activated carbon regenerated by ultrasonic waves coupled with peroxodisulfate has an average particle size of 546 μm. The average particle size has been reduced by 5.86 %, but the activated carbon still has a certain degree of adsorption property. These results also show that the average value of the particle size distribution of the activated carbon is within the range of the particle size, and the particle size distribution curve formed by the regenerated carbon is relatively consistent with that of the new carbon and is relatively smooth, which indicates that the activated carbon is generally in a regular shape under the regeneration effect of ultrasonic waves and does not exhibit much breakage phenomena.

As shown in Fig. 8**b**, it can be seen that there is almost no loss of strength of activated carbon after low-power regeneration (90 W), and the average strengths of the activated carbon regenerated at 150 and 210 W decrease by only 1.25 % and 2.16 %, which is still low, while the average strength of the activated carbon regenerated at 270 W decreases from 98.48 % to 95 %, which is a larger degree of reduction compared with that of activated carbon regenerated at low power. The decrease may be due to the high intensity of ultrasonic waves, which lead to the pulverization and crushing of some of the activated carbon. However, in general, the loss of strength of activated carbon after regeneration by ultrasonic waves is small and has no significant effect.

3.5. OFX-degradation pathway

HPLC-MS was used to detect OFX degradation intermediates, and possible degradation pathways were suggested based on the intermediates detected. As shown in the Fig. 9, a total of 11 intermediates were detected, and pathway 1 is based on free radical attack on the pyridine ring. In the presence of •OH, the hydroxyl group is attached to the C-atom to form a new unstable structure, P1 ($m/z = 377$), resulting in the formation of P2 ($m/z = 393$) and P3 ($m/z = 391.95$) to induce further mineralization (Chen et al., 2022). Pathway 2 involves the demethylation of N-methyl piperazine. In the presence of $SO_4^{\bullet-}$, the methyl group attached to the piperazine ring is shed to form P4 ($m/z = 344$), followed by oxidation of the piperazine ring to form P5 ($m/z = 313$) and removal of the piperazine ring to form P6 ($m/z = 102$) (Yu et al., 2017). In pathway 3, OFX first undergoes decarboxylation to form P7 ($m/z = 318$), which is then degraded by cleavage of the piperazine substituent and oxazinyl group to P8 ($m/z = 298$) and P9 ($m/z = 228$) (Pan et al., 2023). In pathway 4, the degradation to P11 ($m/z = 274$) via piperazine cleavage is possible after undergoing decarboxylation (Sun et al., 2023).

Table 2
Particle-size distributions.

Carbon sample	Average surface area particle size (μm)	Average volume particle size (μm)
AC^1	608.583	701.052
AC^2	580.701	661.624
AC^3	546.784	618.758

3.6. Mechanism of the US/PDS system

In order to further confirm the reactive species produced in the US/PDS system, EPR was utilized to confirm the presence of free radicals. DMPO is a spin-trapping agent that is commonly used to trap $SO_4^{\bullet-}$ and •OH radicals (Wang et al., 2017). As shown in Fig. 10**a**, the four-peak signal typical of DMPO-•OH adducts and a six-peak signal typical of DMPO-$SO_4^{\bullet-}$ adducts validates the results of the regeneration experiments. It shows that in the US/PDS system, sulfate and hydroxyl radicals play an important role in degrading the OFX detached from the activated carbon.

Analyzing Fig. 10**b** and Fig. 10**c**, it can be seen that the content of different organic matter in the water after ultrasound regeneration is significantly higher than that after US/PDS treatment. Fig. 10**c** shows that most of the organic matter is removed after synergistic action, and the fluorescence range is greatly reduced, which is attributed to the fact that the strong oxidizing radicals in the regeneration solution are able to oxidize some of the organic matter and mineralize the products directly into carbon dioxide and water, thus affecting the fluorescence characteristics of the organic dissolved substances in different regions.

According to the given mechanism (Fig. 11), the OFX adsorbed on the mesopores of the activated carbon is continuously dislodged by ultrasonic waves, while at the same time, the persulfate is activated by the ultrasonic waves, and the released sulfate and hydroxyl radicals play a role in the degradation of the OFX. As the degradation efficiency increases, the OTC is shed faster, which further improves regeneration efficiency.

4. Conclusions

In this study, a novel method for the regeneration of used activated carbon based on traditional ultrasonic regeneration coupled with persulfate regeneration is proposed.

First, ultrasonic regeneration of activated carbon was carried out at four different power levels, showing that regeneration efficiency was gradually improved with treatment time, and a regeneration efficiency of 45.371 % was achieved when the regeneration time reached 45 min at an ultrasonication power of 210 W. However, at 270 W, the regeneration efficiency showed a decreasing trend after 20 min, which is due to destruction of the activated carbon under excessive power.

Then, the regeneration of activated carbon by US/PDS regeneration technique was performed, and it was found that the coupled technique improved the regeneration efficiency by 5 % over ultrasonication alone. Furthermore, the regeneration solution was sampled during as well as after regeneration, and the intermediate products were analyzed using liquid chromatography, which elucidated the OFX degradation process.

Although more investigations are needed to fully implement this treatment, it is a promising technique to enhance the removal and destruction of organic pollutants. The tested methods can be used to treat large volumes of wastewater, and the regeneration of activated carbon reduces the generation of highly contaminated solid waste.

CRediT authorship contribution statement

Shiwei Gao: Writing – original draft, Investigation, Data curation, Conceptualization. **Zheng Wang:** Supervision, Project administration. **Yannan Jia:** Writing – review & editing, Funding acquisition. **Nannan Xu:** Writing – review & editing. **Lisha Liao:** Writing – review & editing. **Zhiwei Wang:** Visualization, Validation. **Binbin Wu:** Writing – review & editing, Funding acquisition. **Wanting Feng:** Writing – review & editing. **Yuanxiang Shan:** Writing – original draft. **Lingpeng Hu:** Writing – review & editing. **Hongqin Xue:** Writing – review & editing.

Declaration of competing interest

The authors declare that they have no known competing financial

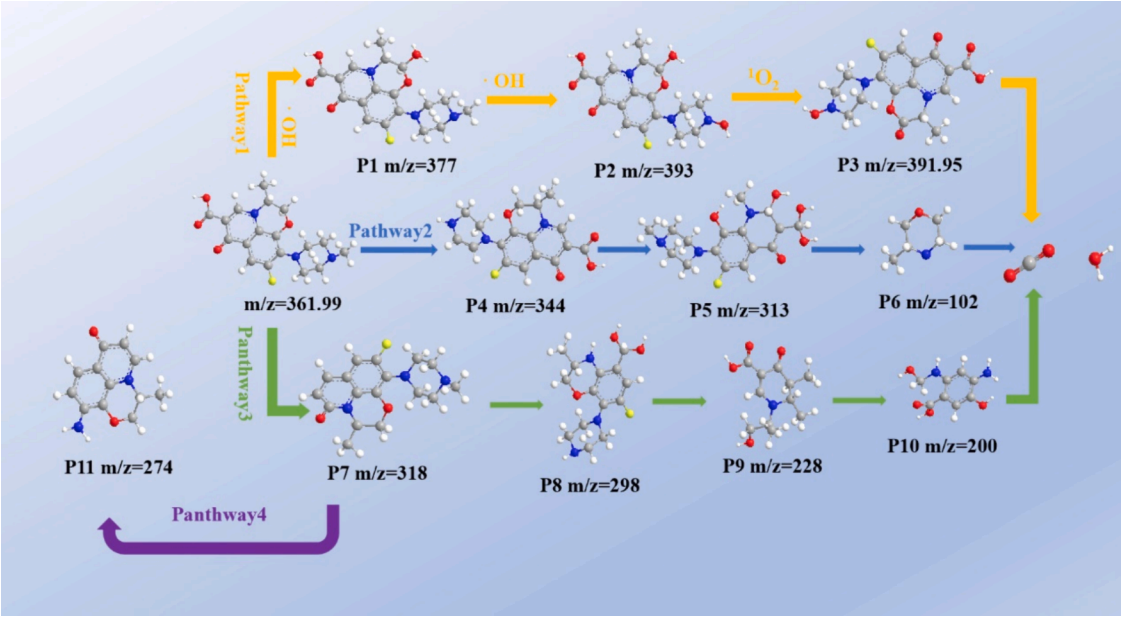

Fig. 9. Proposed OFX degradation pathways.

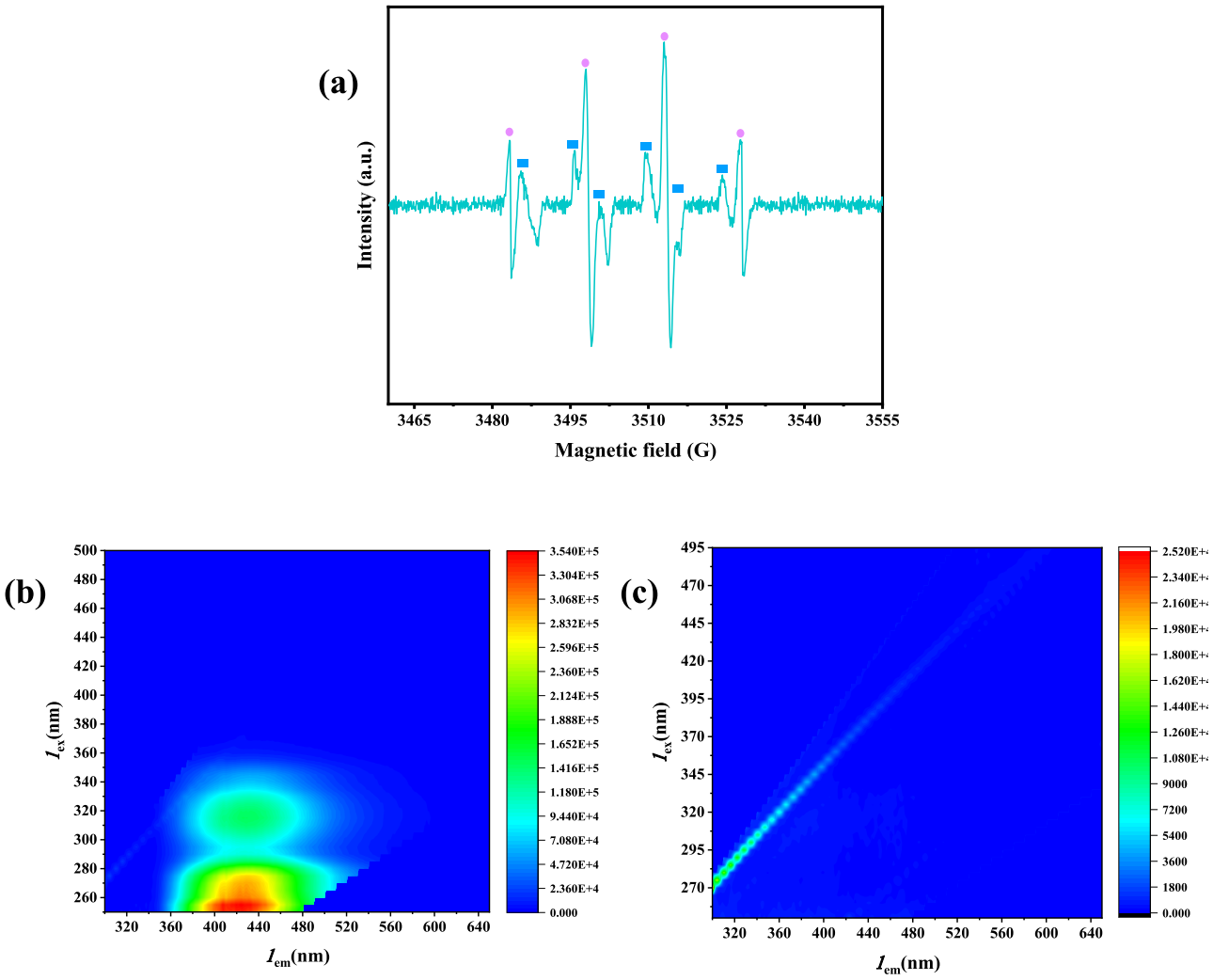

Fig. 10. EPR spectra with DMPO and TEMP: (a) $SO_4^{\bullet-}$ and $^{\bullet}OH$. Three-dimensional fluorescence spectra of (b) ultrasonication backwater; (c) US/PDS backwater.

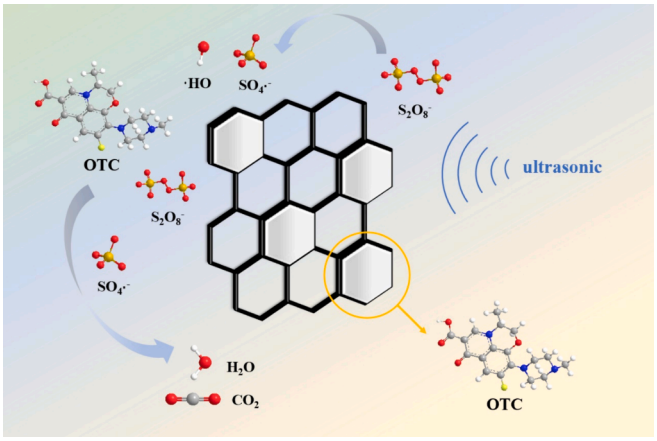

Fig. 11. Proposed mechanism.

interests or personal relationships that could have appeared to influence the work reported in this paper.

Acknowledgments

The authors express their sincere gratitude to the National Key Research and Development Program of China (No. 2023YFC3207901, 2023YFC3207900).

Appendix A. Supplementary data

Supplementary data to this article can be found online at https://doi.org/10.1016/j.arabjc.2024.105929.

References

Babuponnusami, A., Muthukumar, K., 2014. A review on Fenton and improvements to the Fenton process for wastewater treatment. J. Environ. Chem. Eng. 2, 557–572. https://doi.org/10.1016/j.jece.2013.10.011.

Baby, R., Prakash, M.J., 2005. Improving the performance of an active carbon-nitrogen adsorption cryocooler by thermal regeneration. Carbon 43, 2338–2343. https://doi.org/10.1016/j.carbon.2005.04.013.

Beker, U., Ganbold, B., Dertli, H., Gulbayir, D.D., 2010. Adsorption of phenol by activated carbon: Influence of activation methods and solution pH. Energ. Conver. Manage. 51, 235–240. https://doi.org/10.1016/j.enconman.2009.08.035.

Chen, X., Guo, Y., Zhang, H., Cheng, F., Jiao, Z., 2022a. Coke powder improving the performance of desulfurized activated carbon from the cyclic thermal regeneration. Chem. Eng. J. 448, 137459 https://doi.org/10.1016/j.cej.2022.137459.

Chen, Y., Yang, J., Zeng, L., Zhu, M., 2022b. Recent progress on the removal of antibiotic pollutants using photocatalytic oxidation process. Crit. Rev. Environ. Sci. Technol. 52, 1401–1448. https://doi.org/10.1080/10643389.2020.1859289.

Chen, L., Zhou, Z., Shen, C., Xu, Y., 2020. Inactivation of antibiotic-resistant bacteria and antibiotic resistance genes by electrochemical oxidation/electro-Fenton process. Water Sci. Technol. 81, 2221–2231. https://doi.org/10.2166/wst.2020.282.

Cheng, H., Liu, Y., Li, X., 2021. Adsorption performance and mechanism of iron-loaded biochar to methyl orange in the presence of Cr^{6+} from dye wastewater. J. Hazard. Mater. 415 https://doi.org/10.1016/j.jhazmat.2021.125749.

Chowdhury, P., Viraraghavan, T., 2009. Sonochemical degradation of chlorinated organic compounds, phenolic compounds and organic dyes - a review. Sci. Total Environ. 407, 2474–2492. https://doi.org/10.1016/j.scitotenv.2008.12.031.

Ersan, G., Cerron-Calle, G.A., Ersan, G.S.S., 2023. Opportunities for in situ electro-regeneration of organic contaminant-laden carbonaceous adsorbents. Water Res.: J. Int. Water Associat. 232, 119718 https://doi.org/10.1016/j.watres.2023.119718.

Faris, N., Fischmann, A.J., Assmann, S., Jones, L.A., Tardio, J., Madapusi, S., Grocott, S., Bhargava, S., 2021. A study into the behaviour of nickel, cobalt and metal impurities during partial neutralisation of synthetic nickel laterite pressure leach solutions and pulps. Hydrometall. 202, 105604 https://doi.org/10.1016/j.hydromet.2021.105604.

Ge, X., Wu, Z., Cravotto, G., Manzoli, M., Cintas, P., Wu, Z., 2018. Cork wastewater purification in a cooperative flocculation/adsorption process with microwave-regenerated activated carbon. J. Hazard. Mater. 360, 412–419. https://doi.org/10.1016/j.jhazmat.2018.08.022.

Gomez-Rueda, Y., Verougstraete, B., Ranga, C., Perez-Botella, E., Reniers, F., Denayer, J. F., 2022. Rapid temperature swing adsorption using microwave regeneration for carbon capture. Chem. Eng. J. 446, 137345 https://doi.org/10.1016/j.cej.2022.137345.

Guillossou, R., Le Roux, J., Mailler, R., Vulliet, E., Morlay, C., Nauleau, F., Gasperi, J., Rocher, V., 2019. Organic micropollutants in a large wastewater treatment plant: What are the benefits of an advanced treatment by activated carbon adsorption in comparison to conventional treatment? Chemosphere 218, 1050–1060. https://doi.org/10.1016/j.chemosphere.2018.11.182.

Harrower, J., McNaughtan, M., Hunter, C., Hough, R., Zhang, Z., Helwig, K., 2021. Chemical fate and partitioning behavior of antibiotics in the aquatic environment-a review. Environ. Toxicol. Chem. 40, 3275–3298. https://doi.org/10.1002/etc.5191.

Huang, D., Wang, X., Zhang, C., Zeng, G., Peng, Z., Zhou, J., Cheng, M., Wang, R., Hu, Z., Qin, X., 2017. Sorptive removal of ionizable antibiotic sulfamethazine from aqueous solution by graphene oxide-coated biochar nanocomposites: influencing factors and mechanism. Chemosphere 186, 414–421. https://doi.org/10.1016/j.chemosphere.2017.07.154.

Jeon, I.-Y., Choi, H.-J., Jung, S.-M., Seo, J.-M., Kim, M.-J., Dai, L., Baek, J.-B., 2013. Large-scale production of edge-selectively functionalized graphene nanoplatelets via ball milling and their use as metal-free electrocatalysts for oxygen reduction reaction. J. Am. Chem. Soc. 135, 1386–1393. https://doi.org/10.1021/ja3091643.

Jiang, Y., Pétrier, C., Waite, T.D., 2002. Kinetics and mechanisms of ultrasonic degradation of volatile chlorinated aromatics in aqueous solutions. Ultrason. Sonochem. 9, 317–323. https://doi.org/10.1016/s1350-4177(02)00085-8.

Jiang, J., Zhang, S., Longhurst, P., Yang, W., Zheng, S., 2021. Molecular structure characterization of bituminous coal in Northern China via XRD. Raman FTIR Spectrosc. 255, 119724 https://doi.org/10.1016/j.saa.2021.119724.

Lee, J., von Gunten, U., Kim, J.-H., 2020. Persulfate-based advanced oxidation: critical assessment of opportunities and roadblocks. Environ. Sci. Tech. 54, 3064–3081. https://doi.org/10.1021/acs.est.9b07082.

Liu, Y., Cheng, H., He, Y., 2020. Application and mechanism of sludge-based activated carbon for phenol and cyanide removal from bio-treated effluent of coking wastewater. Processes. 8 https://doi.org/10.3390/pr8010082.

Mahamuni, N.N., Pandit, A.B., 2006. Effect of additives on ultrasonic degradation of phenol. Ultrason. Sonochem. 13, 165–174. https://doi.org/10.1016/j.ultsonch.2005.01.004.

Matzek, L.W., Carter, K.E., 2016. Activated persulfate for organic chemical degradation: A review. Chemosphere 151, 178–188. https://doi.org/10.1016/j.chemosphere.2016.02.055.

Miklos, D.B., Remy, C., Jekel, M., Linden, K.G., Drewes, J.E., Huebner, U., 2018. Evaluation of advanced oxidation processes for water and wastewater treatment - A critical review. Water Res. 139, 118–131. https://doi.org/10.1016/j.watres.2018.03.042.

Mourand, J.T., Crittenden, J.C., Hand, D.W., Perram, D.L., Notthakun, S., 1995. Regeneration of spent adsorbents using homogeneous advanced oxidation. Water Environ. Res 67, 355–363. https://doi.org/10.2175/106143095X131583.

Pan, S., Jiang, W., Tian, L., Li, X., Wang, J., Wang, Y., Li, Z., Guo, H., 2023. Simultaneous degradation of antibiotic and removal of phosphate in water by a O_3/CaO_2 advanced oxidation process. Sep. Purif. Technol. 312, 123452 https://doi.org/10.1016/j.seppur.2023.123452.

Pang, Y.L., Abdullah, A.Z., Bhatia, S., 2011. Review on sonochemical methods in the presence of catalysts and chemical additives for treatment of organic pollutants in wastewater. Desalination 277, 1–14. https://doi.org/10.1016/j.desal.2011.04.049.

Robles-Jimenez, L.E., Aranda-Aguirre, E., Castelan-Ortega, O.A., Shettino-Bermudez, B. S., Ortiz-Salinas, R., Miranda, M., Li, X., Angeles-Hernandez, J.C., Vargas-Bello-Pérez, E., Gonzalez-Ronquillo, M., 2021. Worldwide traceability of antibiotic residues from livestock in wastewater and soil: A systematic review. Animals 12, 60. https://doi.org/10.3390/ani12010060.

Rodrigues, L.A., Pinto da Silva, M.L.C., Alvarez-Mendes, M.O., Coutinho, A.d.R., Thim, G. P., 2011. Phenol removal from aqueous solution by activated carbon produced from avocado kernel seeds. Chem. Eng. J. 174, 49–57. https://doi.org/10.1016/j.cej.2011.08.027.

Sadezky, A., Muckenhuber, H., Grothe, H., Niessner, R., Pöschl, U., 2005. Raman micro spectroscopy of soot and related carbonaceous materials: Spectral analysis and structural information. Carbon 43, 1731–1742. https://doi.org/10.1016/j.carbon.2005.02.018.

Salvador, F., Martin-Sanchez, N., Jesus Sanchez-Montero, M., Montero, J., Izquierdo, C., 2013. Regeneration of activated carbons contaminated by phenol using supercritical water. J. Supercrit. Fluids 74, 1–7. https://doi.org/10.1016/j.supflu.2012.11.025.

Sanchez-Yepes, A., Santos, A., Rosas, J.M., Rodriguez-Mirasol, J., Cordero, T., Lorenzo, D., 2023a. Sustainable reuse of toxic spent granular activated carbon by heterogeneous fenton reaction intensified by temperature changes. Chemosphere 341, 140047. https://doi.org/10.1016/j.chemosphere.2023.140047.

Sanchez-Yepes, A., Santos, A., Rosas, J.M., Rodriguez-Mirasol, J., Cordero, T., Lorenzo, D., 2023b. Sustainable reuse of toxic spent granular activated carbon by heterogeneous fenton reaction intensified by temperature changes. Chemosphere 341, 140047. https://doi.org/10.1016/j.chemosphere.2023.140047.

Spessato, L., Bedin, K.C., Cazetta, A.L., Souza, I.P.A.F., Duarte, V.A., Crespo, L.H.S., Silva, M.C., Pontes, R.M., Almeida, V.C., 2019. KOH-super activated carbon from biomass waste: Insights into the paracetamol adsorption mechanism and thermal regeneration cycles. J. Hazard. Mater. 371, 499–505. https://doi.org/10.1016/j.jhazmat.2019.02.102.

Sun, Z., Liu, C., Cao, Z., Chen, W., 2018. Study on regeneration effect and mechanism of high-frequency ultrasound on biological activated carbon. Ultrason. Sonochem. 44, 86–96. https://doi.org/10.1016/j.ultsonch.2018.01.024.

Sun, R., Liu, J., Wu, Y., Xing, S., 2023. Enhanced non-radical degradation of organic pollutants by peroxymonosulfate activation with Zr-Mn composite oxide. Chem. Eng. J. 471, 144529 https://doi.org/10.1016/j.cej.2023.144529.

Sun, F., Yang, C., Qu, Z., Zhou, W., Ding, Y., Gao, J., Zhao, G., Xing, D., Lu, Y., 2021. Inexpensive activated coke electrocatalyst for high-efficiency hydrogen peroxide

production: Coupling effects of amorphous carbon cluster and oxygen dopant. Appl. Catal. B 286, 119860. https://doi.org/10.1016/j.apcatb.2020.119860.
Waclawek, S., Lutze, H.V., Grubel, K., Padil, V.V.T., Cernik, M., Dionysiou, D.D., 2017. Chemistry of persulfates in water and wastewater treatment: A review. Chem. Eng. J. 330, 44–62. https://doi.org/10.1016/j.cej.2017.07.132.
Wang, H., Guo, W., Liu, B., Wu, Q., Luo, H., Zhao, Q., Si, Q., Sseguya, F., Ren, N., 2019a. Edge-nitrogenated biochar for efficient peroxydisulfate activation: An electron transfer mechanism. Water Res. 160, 405–414. https://doi.org/10.1016/j.watres.2019.05.059.
Wang, L., Lu, W., Ni, D., Xu, T., Li, N., Zhu, Z., Chen, H., Chen, W., 2017. Solar-initiated photocatalytic degradation of carbamazepine on excited-state hexadecachlorophthalocyanine in the presence of peroxymonosulfate. Chem. Eng. J. 330, 625–634. https://doi.org/10.1016/j.cej.2017.07.172.
Wang, S., Ning, Z., Si, W., Qi, Z., Zhi, Y., 2015. Modeling the oxidation kinetics of sono-activated persulfate's process on the degradation of humic acid. Ultrason. Sonochem. 23, 128–134. https://doi.org/10.1016/j.ultsonch.2014.10.026.
Wang, H., Sun, F., Qu, Z., Wang, K., Wang, L., Pi, X., Gao, J., Zhao, G., 2019b. Oxygen functional group modification of cellulose-derived hard carbon for enhanced sodium ion storage. ACS Sustain. Chem. Eng. 7, 18554–18565. https://doi.org/10.1021/acssuschemeng.9b04676.
Wang, J., Wang, S., 2020. Reactive species in advanced oxidation processes: formation, identification and reaction mechanism. Chem. Eng. J. 401, 126158 https://doi.org/10.1016/j.cej.2020.126158.
Ye, X., Cai, W., Lu, D., Liu, R., Wu, Y., Wang, Y., 2022. Electrochemical regeneration of granular activated carbon using an AQS (9, 10-anthraquinone-2-sulfonic acid)/PPy modified graphite plate cathode. Chemosphere 308, 136189. https://doi.org/10.1016/j.chemosphere.2022.136189.
Yin, R., Jing, B., He, S., Hu, J., Zhu, M., 2020. Near-infrared light to heat conversion in peroxydisulfate activation with MoS_2: A new photo-activation process for water treatment. Water Res. 190, 116720 https://doi.org/10.1016/j.watres.2020.116720.
Yu, H., Chen, J., Xie, H., Ge, P., Kong, Q., Luo, Y., 2017. Ferrate(VI) initiated oxidative degradation mechanisms clarified by DFT calculations: a case for sulfamethoxazole. Environ. Sci.-Process. Impacts. 19, 370–378. https://doi.org/10.1039/c6em00521g.
Zhang, H.P., 2002. Regeneration of exhausted activated carbon by electrochemical method. Chem. Eng. J. 85, 81–85. https://doi.org/10.1016/s1385-8947(01)00176-0.
Zhang, Q., Zhang, M., Li, T., Du, R., Yu, G., Deng, S., 2023. FeOCl-confined activated carbon for improving intraparticle Fenton-like oxidation regeneration. J. Hazard. Mater. 442, 130026 https://doi.org/10.1016/j.jhazmat.2022.130026.
Zhao, Y., Yuan, X., Li, X., Jiang, L., Wang, H., 2021. Burgeoning prospects of biochar and its composite in persulfate-advanced oxidation process. J. Hazard. Mater. 409, 124893 https://doi.org/10.1016/j.jhazmat.2020.124893.